Journal of Advanced Ceramics
先进陶瓷
ISSN 2226-4108
CN 10-1154/TQ
清华大学出版社 Tsinghua University Press
SciOpen

J Adv Ceram 2026, **15**: 9221412

https://doi.org/10.26599/JAC.2026.9221412

Research Article

A-site cation vacancy engineering in Co-free high-entropy perovskite anodes for high-rate and durable lithium-ion storage

Aiqin Mao[1,*], Feilong Yin[1], Zhengbing Wei[1], Meiyi Pan[1], Shibiao Xu[1], Qianqian Hu[1], Xuefeng Liu[2,*], Zhenxing Yin[3]

[1] *Advanced Ceramics Research Center, School of Materials Science and Engineering, Anhui University of Technology, Ma'anshan 243032, China;*

[2] *College of Chemistry and Pharmaceutical Engineering, Nanyang Normal University, Nanyang 473061, China.*

[3] *School of Metallurgical Engineering, Anhui University of Technology, Maanshan 243032, China.*

* Corresponding author.
E-mail address: A. Mao, maoaiqin@ahut.edu.cn;
X. Liu, liuxuefeng@nynu.edu.cn

Just Accepted

Received: August 14, 2026; Revised: October 29, 2026; Accepted: November 18, 2026

©The Author(s) 2026

Just Accepted

Abstract: High-entropy perovskite oxides (HEPOs) have been positioned as a promising candidate for lithium-ion battery anodes due to their entropy-driven structural robustness and compositional flexibility. However, their inherently low electronic conductivity severely limits practical application by impeding charge transfer and rate capability. Herein, we propose an inactive A-site cation vacancy engineering for Co-free HEPOs, realized through precise stoichiometric tuning of $La_x(Cr_{0.2}Mn_{0.2}Fe_{0.2}Ni_{0.2}Zn_{0.2})O_{3-\delta}$. This approach generates La^{3+} vacancies without sacrificing the redox-active B-site cations, and the resulting charge imbalance is spontaneously compensated by two mechanisms, B-site valence changes and oxygen vacancy formation, thereby synergistically overcoming the conductivity and kinetics limitations. Combined experimental and theoretical investigations reveal that A-site La vacancies serve as favorable Li^+ adsorption sites and fast ion diffusion channels, while the coexisting oxygen vacancies further optimize the electronic structure by enriching O 2p states near the Fermi level. Benefiting from these advantages, the optimized $La_{0.8}(Cr_{0.2}Fe_{0.2}Mn_{0.2}Ni_{0.2}Zn_{0.2})O_{3-\delta}$ electrode delivers 771.4 mAh g^{-1} at 0.2 A g^{-1} (150 cycles), and more notably, achieves a robust high-rate longevity of 602.5 mAh g^{-1} even after 400 cycles at 1 A g^{-1} with a sustained upward capacity trend. This work establishes that engineering cation vacancies

in perovskite-structured HEOs offers an effective and scalable strategy to high-rate and durable anode materials for energy storage application.

Keywords: High-entropy perovskite oxide; A-site cation vacancy; Oxygen vacancy; Reaction kinetics; Lithium-ion battery

1 Introduction

To unlock higher energy and power densities in next-generation lithium-ion batteries (LIBs), the rational design of electrode materials has emerged as a decisive challenge[1]. High-entropy oxides (HEOs), a family of single-phase compounds that host five or more metal cations in equimolar or near-equimolar proportions, offer a compelling platform for addressing this challenge[2-4]. Distinct from conventional transition metal oxides (TMOs), HEOs leverage configurational entropy to stabilize crystal lattices against repeated volume variation, while their multi-component nature offers vast compositional space for electronic structure tailoring[5-8]. Despite these intrinsic merits, their intrinsic electronic conductivity remains poor, exceptionally in micron-sized particles, which severely restricts their application in high-power LIBs.

Defect engineering offers a visible bypass around this constraint by manipulating local atomic structures and coordination environments through the introduction of lattice defects (e.g., cation/anion vacancies, vacancy clusters, and lattice distortions)[9-11]. Among these, anion vacancies are particularly advantageous due to their controllable incorporation and well-documented benefits for electrochemical intercalation [12-14]. For instance, Li et al. constructed a lithium-doped spinel $[Li_{0.1}(CrMnFeCoCu)_{0.9}]_3O_4$ HEO anode, in which the incorporation of low-valent Li^+

Just Accepted

elevates the oxidation states of transition metal while generating abundant oxygen vacancies (O_v), which enhance Li^+ diffusion kinetics and provide additional active sites[12]. Similarly, Liu et al. reported an oxygen-deficient high-entropy perovskite oxide (HEPO), La(FeCoNiCrMn)O_{3-x}, where O_v promote Li^+ adsorption, diffusion and insertion/extraction through unsaturated coordination bonds, local built-in electric fields, and additional diffusion pathways[13]. While these studies validate the efficacy of anion vacancy engineering, strategies centered solely on oxygen vacancies face inherent limits in tuning electronic structures and creating additional ion diffusion channels, motivating the exploration of complementary defect motifs.

In contrast, cation vacancies, another type of classical defects, have received extensive attention in conventional TMOs for electrochemical energy storage[15-19]. As reviewed by Gao et al., deliberately introducing cation vacancies can enhance electronic conductivity, lower ion diffusion barrier, and provide extra charge storage sites[15]. However, cation vacancy engineering in HEOs remains in its early stage[20-22], with fundamental gaps in controllable synthesis and mechanistic understanding. Recently, Xu et al. demonstrated the beneficial effects of B-site cation vacancies in HEPO La($Cr_{0.2}Fe_{0.2}Mn_{0.2}Ni_{0.2}Cu_x\square_{0.2-x}$)$O_{3-\delta}$ on electrochemical performance[22]. Critically, however, B-site cations (such as Cr, Fe, Mn, Ni, and Cu) in perovskite-type HEOs are the redox-active centers, and increasing their vacancies inevitably reduces theoretical specific capacity of the material. In sharp contrast, the A-site rare-earth cations (such as La) are electrochemical inactivity toward Li^+ storage, and introducing inactive A-site cation vacancies does not alter the redox-active species of the B-site

Just Accepted

sublattice. This distinction is supported by non-high-entropy perovskites: an A-site Ce-deficient perovskite $CeNb_3O_9$ anode delivers a sufficient amount of lithium at a high charge/discharge rate, partly owing to the A-site-cation-vacancy-enhanced 3D conduction networks for lithium ions[23], and a similar phenomenon was found in the A-site La/Ce-vacancies $LaCeNb_6O_{18}$ anode in Li^+-Storage[24]. Although these demonstrations are based on non-high-entropy perovskites, they establish A-site vacancy engineering as an effective means of tuning the local coordination environment and ionic transport without sacrificing the redox-active B-site sublattice. The principle is equally, if not more, applicable to high-entropy systems. In HEOs, the presence of multiple A-site rare-earth cations and the resulting configurational entropy not only stabilize the single-phase perovskite structure but also offer a broader compositional space for deliberately introducing A-site vacancies, thereby providing additional freedom to tailor the electronic structure, Li^+ adsorption, and ion-transport kinetics beyond what is achievable in simple perovskites. Therefore, developing A-site inactive cation-deficient HEPO materials to exploit cation vacancies for tuning electronic and crystal structures represents a compelling strategy toward enhanced electrochemical intercalation capabilities.

In this study, we develop an A-site inactive cation-vacancy engineering strategy into a cobalt-free HEPO, $La(Cr_{0.2}Mn_{0.2}Fe_{0.2}Ni_{0.2}Zn_{0.2})O_3$, as a model system[25, 26]. Specially, a series of $La_x(Cr_{0.2}Mn_{0.2}Fe_{0.2}Ni_{0.2}Zn_{0.2})O_{3-\delta}$ (x=1.0, 0.9, 0.8, and 0.7) with controlled La^{3+} deficiency are synthesized via a scalable solution combustion synthesis (SCS) route, enabling systematic tuning of A-site cation vacancies and concomitant

Just Accepted

oxygen vacancies while preserving single-phase perovskite integrity. Among them, the $La_{0.8}(Cr_{0.2}Mn_{0.2}Fe_{0.2}Ni_{0.2}Zn_{0.2})O_{3-\delta}$ composition stands out, where the concerted action of La^{3+} and oxygen vacancies affords markedly improved charge transfer efficiency, rapid electron/Li^{+} transport, and exceptional surface-controlled capacitive behavior.

2 Experiments

2.1 Synthesis of HEPOs

Following our previous procedure[11, 27], a series of $La_x(Cr_{0.2}Mn_{0.2}Fe_{0.2}Ni_{0.2}Zn_{0.2})O_{3-\delta}$ (x=1.0, 0.9, 0.8, and 0.7) HEPOs were synthesized via a simple SCS approach. Stoichiometric quantities of metal nitrates ($La(NO_3)_3\cdot 6H_2O$, $Mn(NO_3)_2\cdot 4H_2O$, $Fe(NO_3)_3\cdot 9H_2O$, $Cr(NO_3)_3\cdot 9H_2O$, $Ni(NO_3)_2\cdot 6H_2O$, and $Zn(NO_3)_2\cdot 6H_2O$; all analytical grade, Sinopharm Chemical Reagent Co., Ltd.) were dissolved in deionized water containing glycine ($C_2H_5NO_2$) as the combustion fuel. The A-site stoichiometry was tuned by mixing 2 mL of each 0.625 M transition metal nitrate solution with a stoichiometric amount of 0.625 M $La(NO_3)_3\cdot 6H_2O$ solution. The fuel–to–oxidizer ratio (φ) was fixed at 0.75, with the required glycine amount determined by the combustion reaction equation:

$$M^{v}(NO_3)_v + \frac{5}{4}v(\varphi-1)O_2 + \frac{5}{9}v\varphi C_2H_5NO_2 \rightarrow M^{v}O_{\frac{v}{2}} + \frac{25}{18}v\varphi H_2O + v\left(\frac{5\varphi+9}{18}\right)N_2 + \frac{10}{9}v\varphi CO_2$$

where Mv represents a metal ion with valence v. The precursor solution was magnetically stirred at room temperature for 1 h to ensure homogeneity, then heated at 80 °C to form a viscous gel. Subsequently, the gel was annealed in a preheated furnace at 750 °C for 30 min, after which the perovskite powders were obtained. The resulting samples (x=1.0, 0.9, 0.8, and 0.7) are hereafter denoted as La0.7, La0.8, La0.9, and La1,

Just Accepted

respectively.

2.2 Material characterization

The crystal structures of the as-synthesized samples were characterized by X-ray diffraction (XRD, Rigaku MiniFlex 600), with Rietveld refinements conducted via the GSAS package. The morphology and elemental homogeneity were examined on a Hitachi S-3500N scanning electron microscopy (SEM)with an energy-dispersive X-ray spectroscopy (EDS) system (Bruker Nano XFlash Detector 5010). Microstructural characterization was conducted on a JEOL JEM-2010 transmission electron microscope (TEM), with HRTEM image processing performed via Gatan Digital Micrograph and interplanar spacings derived from inverse fast Fourier transform (IFFT) analysis. The Brunauer-Emmett-Teller (BET) surface area and Barrett-Joyner-Halenda (BJH) pore size distribution were derived from N_2 adsorption/desorption isotherms measured on a JW-BK200 instrument. X-ray photoelectron spectroscopy (XPS; Thermo Scientific K-Alpha), electron paramagnetic resonance (EPR; Bruker EMXplus), and a four-point probe method (RTS-4) were used for surface chemical analysis, oxygen vacancy detection, and electrical resistivity measurements, respectively.

2.3 Electrochemical characterization

To assess the Li^+ storage performance, CR2025 coin cells were fabricated in a glovebox (MIKROUNA super-750) under an argon atmosphere (H_2O/O_2<0.01 ppm). The working electrodes were prepared by pasting a homogeneous aqueous slurry composed of active material, Super P, and sodium alginate binder in a weight ratio of 7:2:1. These coated foils were then vacuum-dried at 80 °C for 12 h and cut into 14 mm-

Just Accepted

diameter disks, achieving an active mass loading of approximately 1.2–1.5 mg·cm^{-2}. Metallic lithium foil (15.6 mm in diameter) and a Celgard 2500 polypropylene membrane were employed as the counter/reference electrode and the separator, respectively. The electrolyte consisted of 1 M $LiPF_6$ dissolved in a ternary solvent mixture of DEC, EC, and EMC (1:1:1 by volume), supplied by Nanjing Mojes Energy Technology Co., Ltd.

Galvanostatic charge/discharge cycling and galvanostatic intermittent titration (GITT) measurements were conducted using a Neware CT-4008T-5V 10mA-64 battery test system within a voltage window of 0.01–3.0 V (*vs.* Li^+/Li). For GITT, each titration step involved a 5 min constant-current discharge pulse at 200 mA·g^{-1}, followed by a 30 min open-circuit relaxation period to allow potential equilibration. Cyclic voltammetry (CV) was performed on a CHI760E electrochemical workstation over a sweep rate range of 0.1 to 1.0 mV·s^{-1}. Electrochemical impedance spectroscopy (EIS) was also carried out using the same instrument, with a frequency sweep from 10^5 to 0.01 Hz and an AC amplitude of 5 mV.

2.4 DFT calculation

To elucidate the underlying reaction chemistry at the atomic scale, spin-resolved DFT calculations were executed with the VASP code. The exchange–correlation energy was evaluated using the GGA-based PBE functional, while core–valence interactions were treated by the PAW formalism, employing a 400 eV energy cutoff for plane-wave basis expansion. A 15 Å vacuum layer was incorporated perpendicular to the surface to suppress periodic image artifacts. The Brillouin zone was sampled with a single Γ-

Just Accepted

centered k-point (1×1×1 Monkhorst–Pack grid). Geometry relaxations proceeded until atomic forces converged to less than 0.03 eVÅ^{-1} and energy changes dropped below 1×10^{-5} eV per electronic iteration. Dispersion interactions were accounted for using the DFT-D3 approach with Becke–Johnson damping. Activation barriers and saddle points along the reaction coordinates were located via the CI-NEB technique.

3. Results and discussion

3.1 Structure characterization

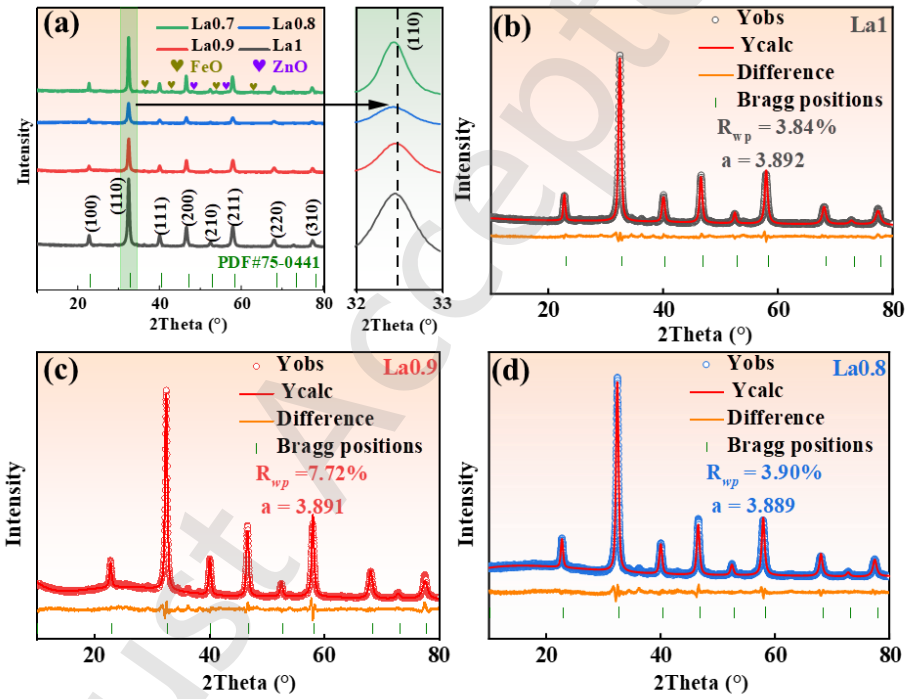


Fig. 1 (a)XRD patterns, and corresponding Rietveld refined XRD patterns of La1 (b), La0.9 (c) and La0.8 (d).

The XRD patterns in Figure 1(a) confirm that the La1, La0.9, and La0.8 samples are phase-pure, with all diffraction peaks indexed to the cubic perovskite structure of $LaCrO_3$ (PDF#75-0441) in the *Pm-3m* space group. When the A-site deficiency increases to 30% (La0.7), ZnO and FeO impurities appear alongside the main

Just Accepted

perovskite phase. This suggests that the perovskite lattice can no longer accommodate the excessive structural distortion and electrostatic repulsion arising from the excessive theoretical La cation vacancies together with the O_V, leading to thermodynamically driven phase separation[17]. Thus, La0.8 represents the critical threshold for vacancy engineering, achieving maximum defect concentration while preserving the structural integrity of the high-entropy perovskite framework [13, 28]. The enlarged (110) diffraction peak progressively shifts to higher 2θ angles as the A-site deficiency increases from La1 to La0.8, indicating a lattice contraction induced by the introduction of La^{3+} vacancies. For La0.7, however, the (110) peak shifts to a lower angle relative to La0.8 sample. This anomalous behavior is attributed to the exsolution of B-site metal ions and the resulting compositional change within the remaining perovskite lattice, rather than a further increase in vacancy concentration.

Rietveld refinements against the diffraction data for the single-phase samples La1, La0.9, La0.8 are presented in Fig. 1b–d, while Table S1 (Supporting Information) lists all derived structural parameters. Low weighted profile *R*-factor (R_{wp}) and χ^2 values attest to the refinement quality. Notably, the lattice parameters shrink systematically upon progressive La-vacancy introduction (3.892, 3.891, and 3.889 Å for La1, La0.9, and La0.8, respectively), quantitatively mirroring the gradual (110) peak shift observed in Fig. 1(a). The detailed atomic positions and site occupancies are summarized in Tables S2–S4 (Supporting Information). La occupies the A-site (1a), Cr, Mn, Fe, Ni, and Zn are mixed at the B-site (1b), and O occupies 3d sites. By regulating the La ratio (x=1.0, 0.9, 0.8), the La1, La0.9 and La0.8 samples exhibit decreasing La-site

Just Accepted

occupancies of 99%, 92% and 87%, and O-site occupancies of approximately 85%, 82% and 78%, respectively, confirming the presence of vacancies at both La and O sites in $La_x(Cr_{0.2}Mn_{0.2}Fe_{0.2}Ni_{0.2}Zn_{0.2})O_{3-\delta}$. Specifically, for the La1, La0.9 and La0.8 samples, these occupancies correspond to La-vacancy concentrations of approximately 1%, 8%, and 13%, and O-vacancy concentrations of approximately 15%, 18%, and 22% with equivalent δ values of about 0.45, 0.54, and 0.66, respectively. In sharp contrast, the B-sites are fully occupied in all three samples, confirming that no B-site vacancies are introduced.

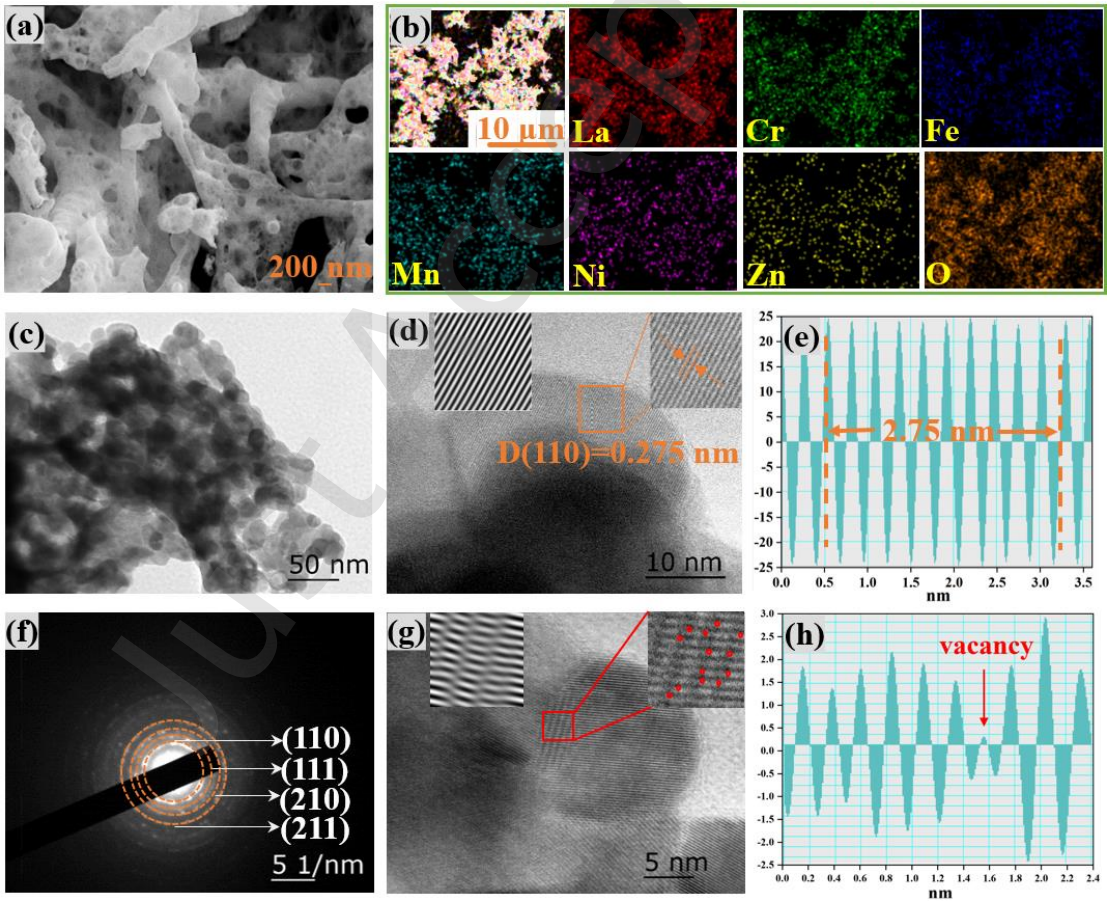


Fig. 2 (a) SEM image and (b) corresponding elemental mappings; (c) TEM image, (d, g) HRTEM images with insets showing the IFFT image, (e, h) profile plot of the atomic array, and (f) SAED pattern of La0.8 sample.

The morphology and microstructure of the three single-phase HEPOs were systematically investigated by SEM and TEM. As shown in Fig. 2a, the La0.8 sample exhibits a typical three-dimensional (3D) interconnected porous network with a sponge-like architecture, a hallmark of the SCS method arising from massive gas evolution during the violent combustion reaction[27]. Comparative SEM analysis (Fig. S1, Supporting Information) reveals that the introduction of La vacancies does not compromise this porous architecture; instead, the macroscopic morphology is well preserved across the La1, La0.9 and La0.8 samples. Furthermore, EDS mapping (Fig. 2b; Fig. $S1c_1$, $S1c_2$) confirms that all constituent cations are uniformly distributed within the selected micro-regions, indicating no elemental segregation regardless of vacancy concentration. Meanwhile, the elemental compositions at La0.8 broadly consistent with the nominal precursor ratios (Fig. S2, Supporting Information), confirming that no B-site vacancies are introduced, is line with the Rietveld refinements (Table S2-S4).

TEM was employed to probe the fine microstructure of the La0.8 sample. The TEM image (Fig. 2c) reveals a porous architecture assembled from numerous nanoparticles ranging from 10 to 40 nm of La0.8 sample. The HRTEM image (Fig. 2d) displays well-resolved, equally spaced atomic lattice fringes, indicating excellent crystallinity of the sample. The corresponding profile plot (Fig. 2e) yield a precise interplanar spacing of 0.275 nm, matching the (110) plane of perovskite crystal. The SAED pattern (Fig. 2f) exhibits well-defined concentric diffraction rings, which are characteristic of polycrystalline materials. These rings can be indexed from inside to

Just Accepted

outside as the (110), (111), (210), and (211) planes. Meanwhile, in another region imaged at higher magnification (indicated by the red rectangle, Fig. 2g), distinct distinct lattice defect is revealed (marked with red circles) and further confirmed by the line scan profiles in Fig. 2h, where the selected section exhibits irregular intensity fluctuations with distinct minima[20]. Additionally, localized lattice distortions are evident in the IFFT image (insets of Fig. 2g), arising from the elevated concentration of A-site cation vacancies together and the differing ionic sizes among the multi-principal B-site cations. Such appropriate structural distortion not only provides abundant transport pathways for Li^+, but also modulates the electronic structure of the as-synthesized La0.8 anode[29]. Collectively, the HRTEM and SAED results demonstrate that the perovskite crystalline framework remains intact despite the introduction of up to 13% La cation deficiencies and 22% O anion vacancies in La0.8.

To gain insight into the specific surface area and pore architecture, N_2 adsorption–desorption isotherms were recorded for all prepared sample. As evidenced by the Type IV isotherms and H3 hysteresis loops recorded for every sample (Fig. S3, Supporting Information), every sample possesses a mesoporous structure, as further supported by BJH pore-size maxima lying in the 2–10 nm range[30]. Quantitative textural parameters (Table S6, Supporting Information) demonstrate that La0.8 outperforms its counterparts, offering the highest BET surface area (S_{BET}) of 28.89 $m^2 \cdot g^{-1}$ and BJH pore volume (V_{BJH}) of 0.096 $cm^3 \cdot g^{-1}$, concurrently with reduced average and dominant probable pore sizes. Such a highly porous structure with an enlarged surface area is particularly beneficial for electrode materials, as it not only maximizes the electrode–electrolyte contact area

Just Accepted

to facilitate rapid Li^+ transport but also provides effective buffering capacity to accommodate the substantial volume changes during repeated lithiation/delithiation cycles[13].

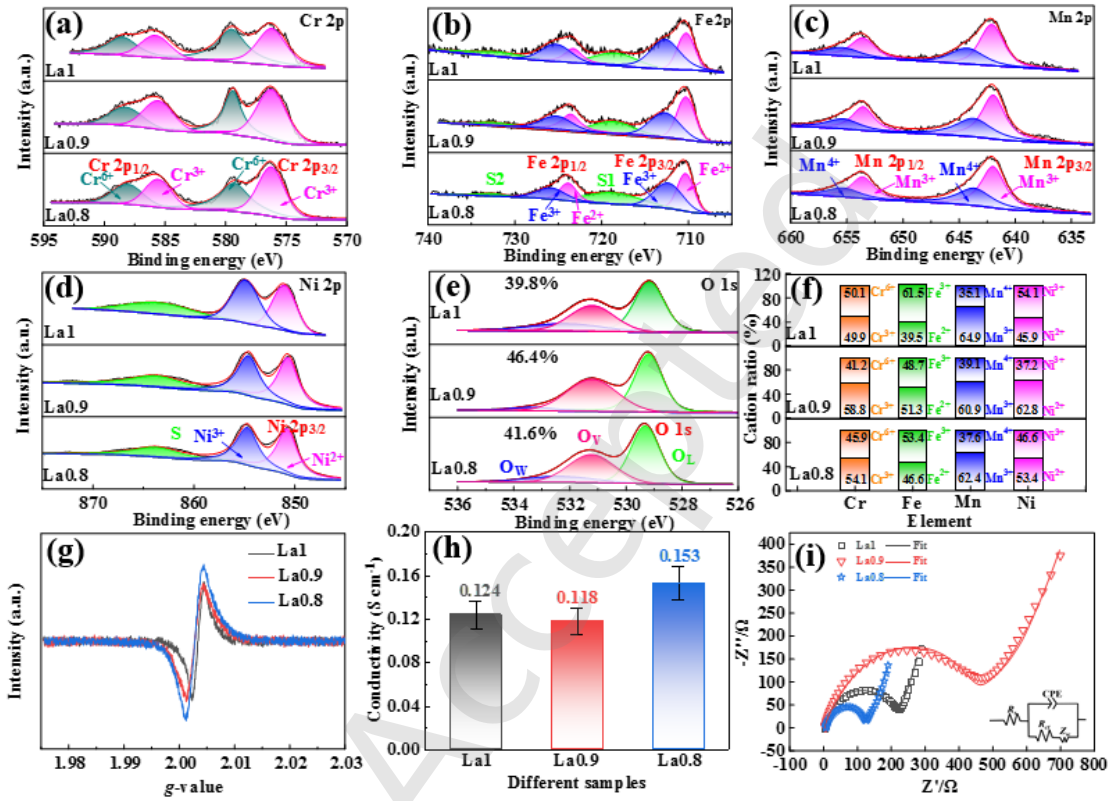


Fig. 3. (a-e) High-resolution XPS spectra, and (f) valence state distributions of metal cation; (g)EPR spectra; (h) electrical conductivity; (i) initial Nyquist plots.

XPS characterization was undertaken to assess the elemental valence configurations and surface oxygen vacancy concentrations of the three single-phase samples. The survey spectra (Fig. S4a, Supporting Information) confirm the expected elemental composition of La, Cr, Mn, Fe, Ni, Zn, and O. In the Cr 2p spectra (Fig. 3a), peaks at 576.3 eV (Cr $2p_{3/2}$) and 585.6 eV (Cr $2p_{1/2}$) are assigned to Cr^{3+}, along with additional peaks at 579.4 and 588.6 eV, attributable to Cr^{6+} [13]. Similarly, the mixed Fe^{2+}/Fe^{3+}, Mn^{3+}/Mn^{4+} and Ni^{2+}/Ni^{3+} states for Fe, Mn and Ni elements are resolved

Just Accepted

from the spectra in Fig. 3b-d. Meanwhile, La and Zn exhibit solely as +3 and +2, respectively (Fig. S4b, c)[13, 31]. Quantitative XPS analysis (Figs. 3e and 3f) shows that the introduction of La vacancies triggers two parallel charge compensation mechanisms: (i) valence changes of the B-site cations (reduction of Cr^{6+}, Fe^{3+} and Ni^{3+}, along with an increase of Mn^{4+}), and (ii) the formation of O_V. Specifically, as the A-site deficiencies increase from La1.0 to La0.9, the fractions of Cr^{6+}, Fe^{3+} and Ni^{3+} decrease, while the relative fraction of the O1s component assigned to oxygen-vacancy-related species increases from 39.8% to 46.4% (Fig. 3e). Interestingly, La0.8 exhibits a lower extent of B-site cation reduction and a lower relative fraction of this O 1s component (41.6%) compared with La0.9. This discrepancy is attributed to spontaneous surface reconstruction under high cation-vacancy concentration: the lattice undergoes structural relaxation to minimize surface energy, redistributing defects between the surface and bulk[32, 33]. These results suggest that A-site La deficiency modifies the defect chemistry and distribution, thereby influencing the local electronic environment of the perovskite.

EPR analysis cross-validated the overall O_V concentration (Fig. 3g), revealing a distinct g=2.003 resonance signal characteristic of oxygen vacancies across all samples, with intensities ranking La0.8>La1>La0.9 in positive correlation with total concentration[34]. The variation trend of overall O_V concentration is consistent with the results of XRD Rietveld refinements (Tables S2–S4, Supporting Information). The electrical conductivity measurements (Fig. 3h) show the same ranking as the EPR signal intensity, with La0.8 exhibits the highest value (0.153 S cm^{-1}), followed by La1 (0.124

Just Accepted

S cm^{-1}) and La0.9 (0.118 S cm^{-1}). Moreover, the Nyquist plots are presented in Fig. 3i and the fitted parameters from the equivalent circuit are summarized in Table S7. La0.8 displays the smallest high-frequency semicircular, indicating a markedly reduced charge transfer resistance (R_{ct}). Specifically, La0.8 shows the smallest R_{ct} (115.1 Ω) compared with La1 (189.4 Ω) and La0.9 (395.8 Ω), showing lower charge-transfer resistance than both La1 and La0.9. These results indicate that La deficiency modifies the defect chemistry and local electronic environment of the perovskite. The changes in B-site cation valence states and oxygen-vacancy-related species may be coupled through electronic redistribution, although their individual contributions to charge compensation cannot be quantitatively determined from XPS and EPR results alone.

3.2 Electrochemical performance

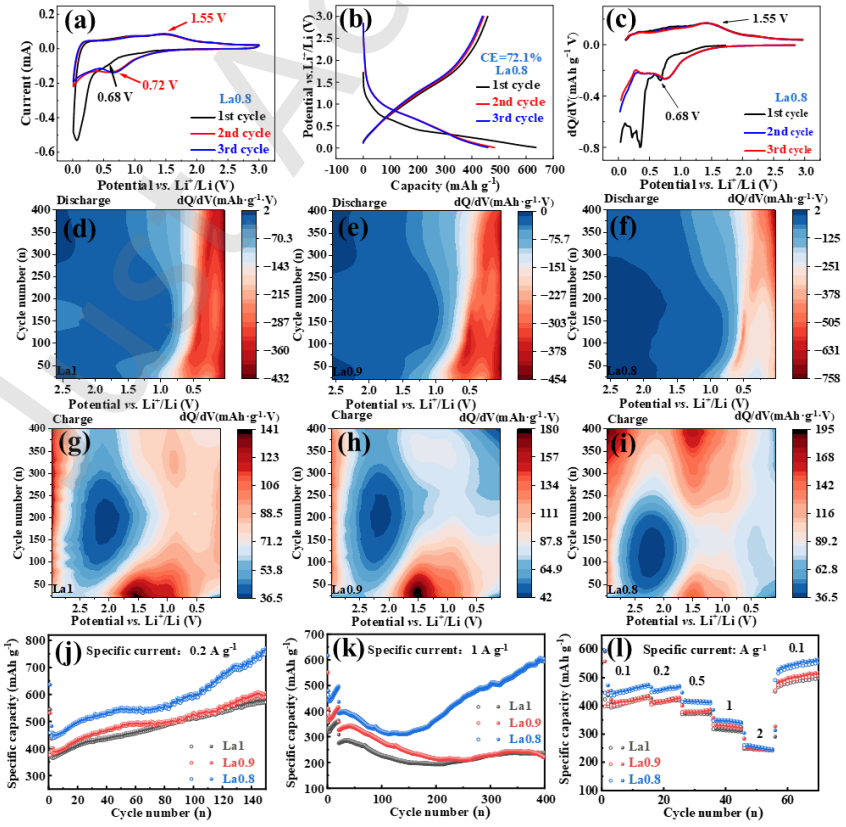


Fig. 4. Electrochemical characterization of the three HEPO electrodes: (a) CV curves

of the initial three cycles at 0.2 mV s^{-1}; (b) galvanostatic charge-discharge profiles at 0.2 A g^{-1}; (c) *dQ/dV* plots for La0.8; (d-i) *d*Q/*d*V contour maps over 150 cycles for La1 (d, g), La0.9 (e, h) and La0.8 (f, i); (j) cycling performance at 0.2 A g^{-1}, (k) long-term cycling at 1 A g^{-1} with an initial activation step of 20 cycles at 0.2 A g^{-1}, and (l) rate capability.

The Li^+-storage properties of the three single-phase HEPOs were systematically evaluated in CR2025-type half-cells. The La0.8 electrode (Fig. 4a) shows a broad and distinct reduction peak at ~0.68 V, attributable to cation reduction, Li_2O formation, and irreversible solid electrolyte interphase (SEI) growth[35]. This peak positively shifts to 0.72 V in later cycles, indicating suggesting activation-induced depolarization. The corresponding oxidation peak appears at 1.55 V, associated with the reversible reoxidation of metallic species. Notably, the CV curves of the second and third cycles exhibit near-perfect overlap, implying excellent electrochemical reversibility of La0.8 electrode [36]. Similar reversible redox behavior is also observed for the pristine La1 (Fig. S5a) and the slightly A-site-deficient La0.9 (Fig. S5d) electrodes.

The initial three charge/discharge profiles of the three HEPO electrodes are presented in Fig. 4b, S4b and S4e. All electrodes exhibit an initial capacity loss, a common feature of conversion-type anodes arising from electrolyte decomposition and SEI formation. Remarkably, the reversible capacity increases progressively with increasing A-site deficiency, indicating that engineered A-site vacancies effectively activate additional intrinsic reactive sites[15]. The well-defined voltage plateaus observed in these profiles align well with the CV redox peaks, as further corroborated

Just Accepted

by differential capacity (dQ/dV) analysis (Fig. 4c, S5c, and S5f). Long-term dQ/dV contour plots (Fig. 4d-i) reveal that La0.8 maintains well-defined redox peaks with minimal polarization over 150 cycles, in sharp contrast to the rapidly fading and severely polarized peaks of La1 and La0.9.

The cycling stability at 0.2 A g^{-1} is presented in Fig. 4j. All three electrodes exhibit a gradual capacity increase during cycling, resulting from enhanced kinetics and progressive activation. EIS (Fig. S8 and Fig. S9) supports this activation by revealing a marked charge-transfer resistance (R_{ct}) decrease after 150 cycles, which points to improved interfacial charge transfer. After 150 cycles, the La0.8 electrode retains a reversible capacity of 771.4 mAh g^{-1}, higher than that of La0.9 (605.5 mAh g^{-1}) and La1 (583.7 mAh g^{-1}). However, further increasing the A-site deficiency to theoretical value of 30% (La0.7) triggers phase separation and a sharp capacity drop to 490.3 mAh g^{-1} after 150 cycles (Fig. S6). Combined with the structural analysis, these results identify La0.8 as the optimal composition for lithium storage. The long-term cycling behavior at 1 A g^{-1} (Fig. 4k) reveals a distinctly upward capacity trend for La0.8, which maintains a high reversible capacity of 602.5 mAh g^{-1} after 400 cycles, significantly outperforming La1(239.1 mAh g^{-1}) and La0.9 (219.5 mAh g^{-1}). Collectively, the optimized La0.8 electrode delivers performance competitive with state-of-the-art perovskite and HEO-based anodes(Table S6, Supporting Information)[13, 26, 37-40]. Furthermore, rate capability comparison (Fig. 4l) shows that the La0.8 electrode delivers a high capacity of 256.1 mAh g^{-1} even at 2 A g^{-1}, outperforming both La0.9 and La1, which indicates faster Li^+ diffusion and reaction kinetics. Moreover, upon

Just Accepted

switching back to low current density, the initial capacity of La0.8 is fully recovered, highlighting its structural robustness and reversibility. This enhanced electrochemical performance originates from the synergistic interplay between A-site La^{3+} cation vacancies and the associated oxygen vacancies. Specially, cation vacancies serve as favorable Li^+ storage sites and preferential transport channels, boosting specific capacity and rate performance [15, 17]. Meanwhile, oxygen vacancies facilitate Li^+ adsorption, diffusion and insertion/extraction through unsaturated coordination bonds, local built-in electric fields, and additional diffusion pathways[13, 41].

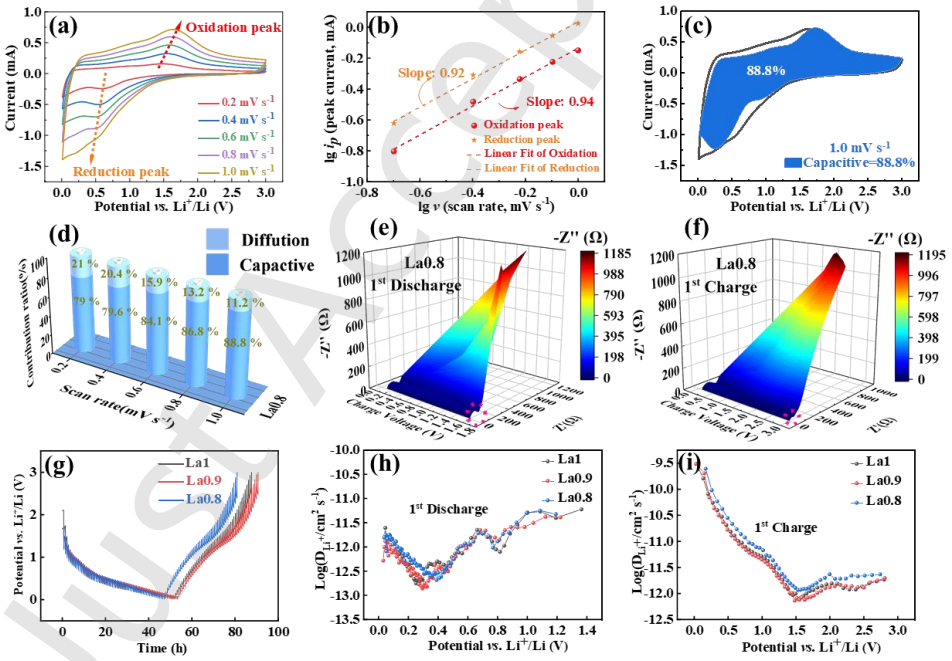


Fig. 5 Kinetic analysis of the as-synthesized HEPO anodes: (a) CV at different scan rates, (b) relationship between lg(i_p) and lg(v), (c) capacitive contribution (shaded region) at 1.0 mV s^{-1}, and (d) capacitive contribution rations at different scan rates during the initial cycle of La0.8 electrode; (e, f) *In situ* EIS spectra of La0.8 electrode; (g) GITT profiles, and (h, i) corresponding Li^+ diffusivity for the three electrodes.

Just Accepted

To elucidate the intrinsic origin of the exceptional rate capability and cycling stability of La0.8 electrode, systematic kinetics analyses were conducted. The CV curves (Fig. 5a, Fig. S5b) reveal that La0.8 exhibits smaller redox peak shifts at higher scan rates, implying lower polarization and faster kinetics. The peak current (i_p) and scan rate (v) are related by the power-law $i_p = av^b$ [42]. From the linear relationship between lg(i) versus lg(v) (Fig. 5b), the calculated b-values for La0.8 are 0.94 (cathodic) and 0.92 (anodic), compared to 0.86 (cathodic) and 0.94 (anodic) for La1. Furthermore, the total current, $i(V)$, can be decoupled into pseudocapacitive (k_1v) and diffusion-controlled ($k_2v^{1/2}$) contributions using $i(V) = k_1v + k_2v^{1/2}$. Quantitative analysis (Fig. 5c, d and Fig. S7c, d) shows that La0.8 delivers significantly higher pseudocapacitive contributions than La1 across all scan rates, ranging from 79.0% to 88.8% at 0.2-1.0 mV s^{-1}, compared to 65.7%-81.1% for La1. These findings provide definitive evidence that A-site non-stoichiometry introduces abundant cation vacancies and appropriate oxygen vacancies as redox active sites, thereby enhancing pseudocapacitive lithium-ion storage[13].

To dynamically track interfacial charge transfer kinetics and SEI film evolution during the 1st cycle, *in situ* EIS was performed on pristine La1 and optimized La0.8 electrodes (Fig. 5e, 5f, Fig. S8). For La0.8 electrode, as lithiation deepens, the rising Li^+ concentration causes a slight increase in R_{ct}. Upon subsequent charging, R_{ct} steadily decreases to 50 Ω at full charge (Fig. S8f, Supporting Information), indicating gradual charge transfer acceleration due to electrochemical activation. Meanwhile, discharge to 1.2 V induces a new high-frequency semicircle (Fig. S8c, Supporting Information),

Just Accepted

evidencing SEI formation[35], consistent with the first-cycle CV peak (Figure 4a). Similar phenomenon is observed for the La1 electrode (Fig. S8a, b, d, e, Supporting Information). Notably, the La0.8 electrode exhibits a smaller R_{ct} than La1, reflecting intrinsically faster interfacial kinetics. This further suggests that A-site vacancies effectively optimize the electronic structure and facilitate charge transfer during the initial activation process[17, 19]. Meanwhile, the Li^+ diffusion coefficients (D_{Li}^+) of the three electrodes were further determined by GITT (Fig. 5g), with the room-temperature D_{Li}^+ values calculated as detailed in Fig. S10 (Supporting Information). As shown in Fig. 5h, i, the La0.8 electrode possesses a higher D_{Li}^+ than both La1 and La0.9. These results highlight that the introduction of A-site vacancies not only improves ionic conductivity but also promotes faster Li^+ transport, which are concurrently critical to the high-rate capability and long-term cycling stability of the La0.8 electrode.

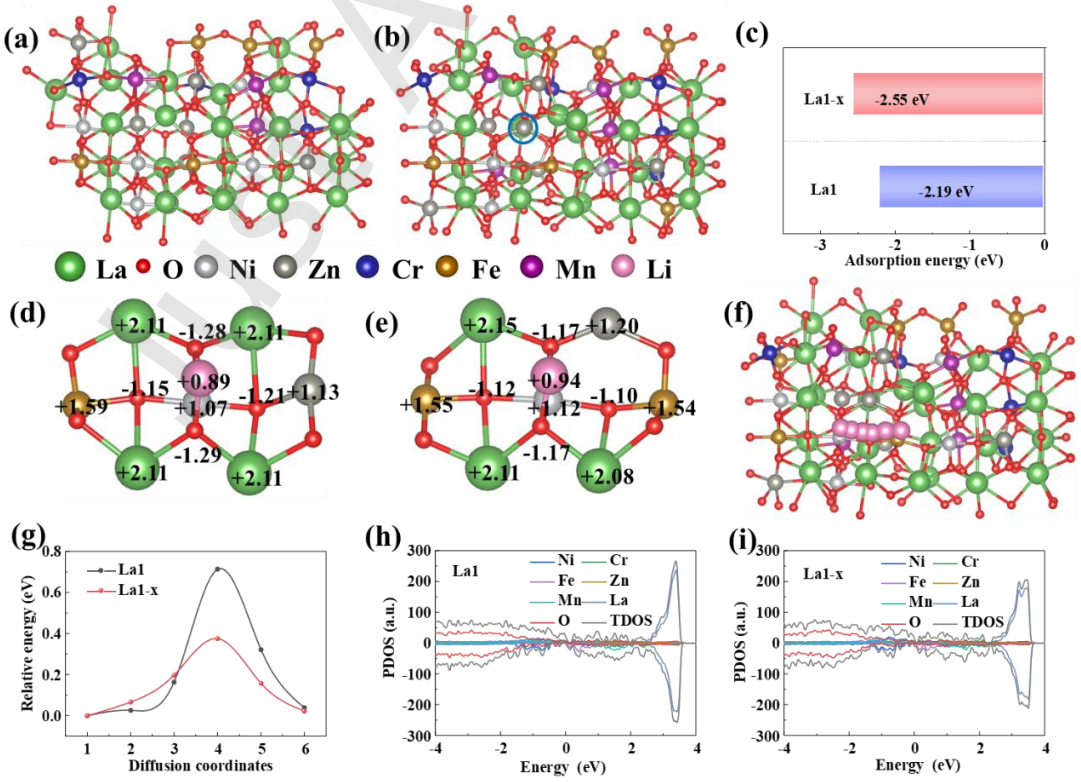


Fig. 6 (a) Perfect La1 and (b) La-deficient La1-x surface models; (c) The calculated Li^+

adsorption energies; (d, e) Bader charge distributions of La1 and La1-x surfaces after Li^+ adsorption; (f) Li^+ migration pathway and (g) the corresponding Li^+ diffusion energy barrier; (h, i) PDOS curves of La1 and La1-x structures.

To reveal the lithium storage enhancement mechanism of A-site La vacancies in perovskite HEOs, we systematically investigated the regulatory effects of La vacancies on interfacial charge transfer and local electronic structure via DFT calculations. Fig. 6a and b present the stoichiometric La1 and non-stoichiometric La1-x surface models, respectively, with the La vacancy indicated by the blue circle. The calculation results of single Li atom adsorption energy (Fig. 6c) show that the Li^+ adsorption energy on the La1-x surface is -2.55 eV, significantly lower than -2.19 eV on the perfect La1 surface. This suggests that the La vacancies remarkably enhances the interaction between Li^+ and the substrate surface, which is beneficial for increasing the surface Li^+ coverage and pseudocapacitive storage capacity. Fig. 6d and e compare the local Bader charge distributions of the two models after Li^+ adsorption. The results demonstrate that on the La1-x surface, the Bader charge of the adsorbed Li^+ atom increases from +0.89 e to +0.94 e, suggesting a higher degree of electron transfer and more complete ionization of Li^+. Meanwhile, the charges of the surrounding O atoms all shift to more positive values, confirming that O atoms undergo oxidation and serve as the primary charge compensation centers, while the adjacent La atoms fine-tune their charges to accommodate the lattice strain induced by the vacancies. This local charge redistribution activates the redox activity of O atoms and simultaneously enhances the charge transfer efficiency of Li^+.

Just Accepted

Fig. 6f and g illustrate the migration pathways and calculated diffusion energy barrier of Li^+ along adjacent transition metal atoms. Compared with the La1 surface (0.71 eV), the diffusion energy barrier of Li^+ on the La1-x surface is only 0.38 eV, demonstrating that La vacancies can significantly reduce the diffusion resistance of Li^+. This can be mainly attributed to the abundant holes generated in the O 2p orbitals after O oxidation, which provide additional low-energy diffusion channels for Li^+. PDOS analysis (Fig. 6h-i) further reveals that the total DOS near the Fermi level increases on the La1-x surface, which is predominantly contributed by the O 2p orbitals. This is consistent with Bader charge analysis that O atoms participate in redox reactions, and also accounts for the higher electronic conductivity of the La1-x sample. In conclusion, the theoretical calculation results consistently confirm that A-site La vacancy engineering significantly improves the lithium storage performance of perovskite HEOs by enhancing Li^+ adsorption, accelerating ion diffusion, and optimizing the electronic structure.

Just Accepted

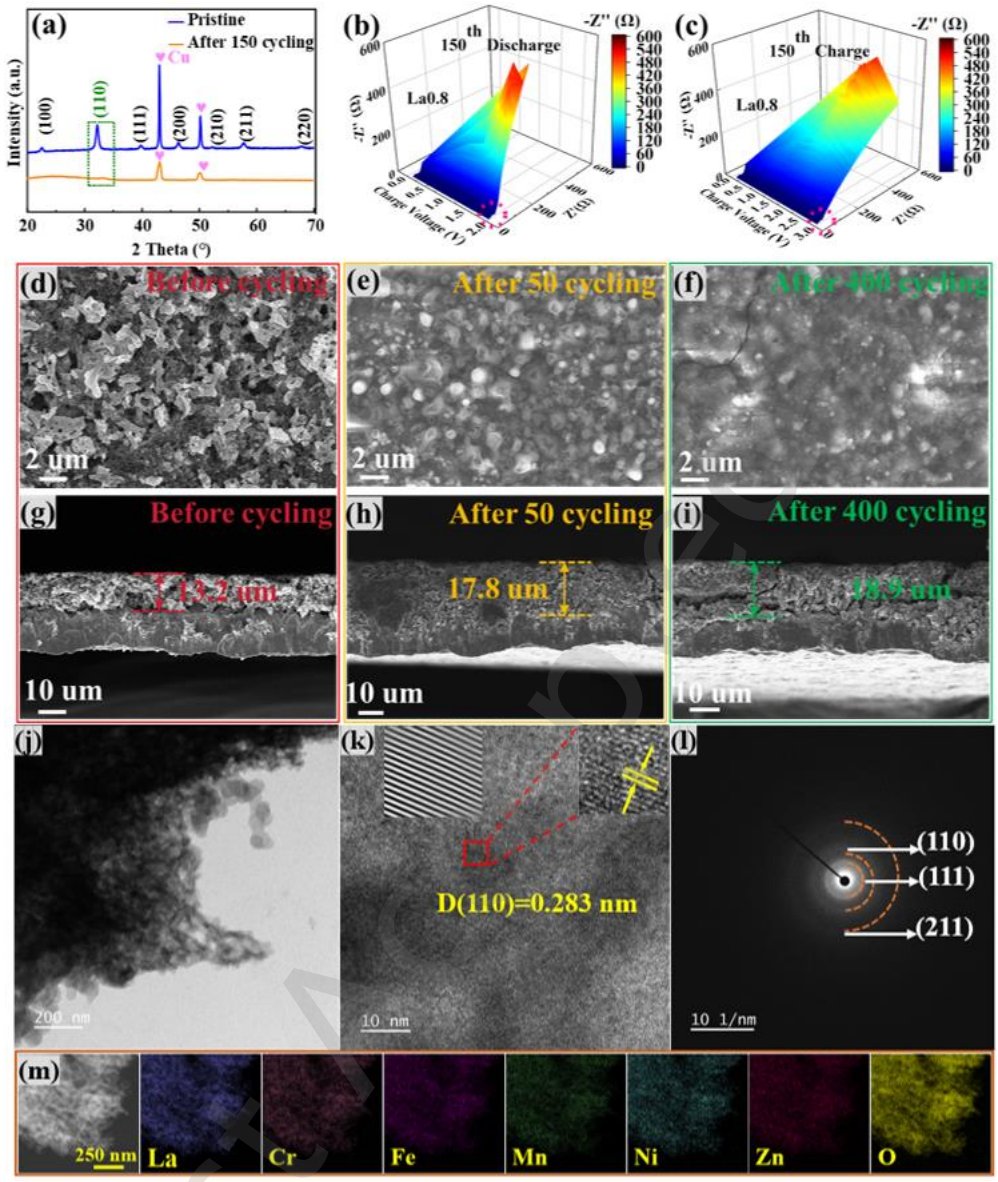


Fig.7 Stability evaluation of La0.8 electrode: (a) XRD analysis of structural integrity pre- and post-cycling (150 cycles at 0.2 A g^{-1}); (b, c) post-cycling *In situ* EIS (150 cycles at 0.2 A g^{-1}); (d–i) SEM images of pristine (d, g), 50-cycle (e, h), and 400-cycle (f, i) at 1 A g^{-1} in top-view (d–f) and cross-sectional (g–i); (j) TEM images, (k) HRTEM image, (l) SAED pattern, and (m)EDS mapping after 400 cycles.

To unravel the mechanism of reversible Li^+ storage, the structural evolution of La0.8 after cycling was investigated by *ex-situ* XRD, *in situ* EIS, SEM and TEM (Fig.

7). As shown in Fig. 7a, the pristine crystal framework undergoes significant structural reconstruction during cycling. Most initial diffraction peaks gradually attenuate, with only the (110) characteristic peak retained after 150 cycles. The intensity of this diffraction peak decreases markedly accompanied by peak broadening, indicative of a substantial decline in crystallinity and grain refinement upon long-term cycling. Such structural reconstruction exposes abundant active surfaces, continuously boosting the pseudocapacitive contribution and thus enabling the progressive increase in lithium storage capacity[43]. Additionally, 3D *in situ* EIS characterization was collected on La1 and La0.8 electrodes during the 150th charge–discharge cycle (Fig. 7b, c and Fig. S9). The R_{ct} decreases markedly relative to its initial value, signaling enhanced redox kinetics after prolonged activation. Meanwhile, the near-constant R_{ct} and R_{SEI} values confirm a stable SEI layer and sustained structural integrity over extended cycling.

The micromorphology and volume change of the electrode were monitored by SEM. As shown in Fig. 7d, the fresh electrode possesses a porous architecture with active particles evenly distributed throughout. Following 50 cycles (Fig. 7e, h), the particles still retain good dispersion, yet a discernible SEI film becomes apparent on the surface. Upon 400 long cycles, the original porous framework is almost fully covered by a thick and dense SEI film (Fig. 7f). Cross-sectional SEM analysis (Fig. 7g–i) shows that the electrode thickness expands from 13.2 μm to 17.8 μm after 50 cycles (34.8% increase, ~0.70% per cycle). This expansion, in turn, induces SEI cracking and fresh surface exposure, which are responsible for the capacity fluctuation in the early stage. Upon reaching 400 cycles, the thickness rises further to 18.9 μm, marking a

Just Accepted

cumulative swelling of 43.2%. This suggests that volume expansion predominantly occurs within the initial 50 cycles, while the subsequent volumetric strain is remarkably suppressed by the porous structure and high-entropy lattice. This self-limiting expansion behavior is the key to maintaining structural integrity and stable capacity during long-term cycling.

Furthermore, TEM analysis was performed on the active materials after 400 cycles (Fig. 7j-m). The TEM image (Fig. 7j) reveals the formation of ultrafine grains. Meanwhile, the well-resolved lattice fringes in the HRTEM image (Fig. 7k) and the partial diffraction rings in the SAED pattern (Fig. 7l) provide unambiguous evidence that the perovskite host framework survives extended cycling, in agreement with the XRD results for La0.8 after 150 cycles. Notably, the (110) interplanar spacing expands from 2.75 Å in the pristine state (Fig. 2g) to 2.83 Å after 400 cycles (Fig. 7k), which is attributable to the irreversible insertion of Li^+ into the lattice. In addition, HRTEM-EDS mapping (Fig. 7m) reveals uniform La, Cr, Mn, Fe, Ni and Zn distribution within the La0.8 without detectable segregation. Generally speaking, the limited volume expansion, grain refinement, and preserved perovskite structure after 400 cycles substantiate the enhanced capacity and cycling stability of the La0.8 electrode with a controlled concentration of La and O vacancies.

4 Conclusion

In summary, this work systematically demonstrates that A-site cation vacancy engineering via non-stoichiometry design overcomes the intrinsic conductivity limitations of HEPO anodes, enabling high-rate and durable lithium-ion storage. Taking

Just Accepted

cobalt-free $La_x(Cr_{0.2}Mn_{0.2}Fe_{0.2}Ni_{0.2}Zn_{0.2})O_{3-\delta}$ as a model system, we demonstrate that A-site La^{3+} deficiency enables the synergistic regulation of cation vacancies and oxygen vacancies through two charge compensation mechanisms: valence changes of B-site cations and the generation of oxygen vacancies. Among the series, the optimized La0.8 electrode achieves the critical threshold for maximum defect concentration while preserving single-phase structural integrity. Combined experimental characterizations and DFT calculations reveal that these A-site vacancies synergistically enhance Li^+ adsorption (−2.55 eV *vs.* −2.19 eV on La1), accelerate Li^+ diffusion (0.38 eV *vs.* 0.71 eV energy barrier), and optimize the electronic structure via O 2p-dominated states near the Fermi level. Consequently, the La0.8 electrode delivers superior specific capacity, outstanding rate capability, and remarkable cycle stability over 400 cycles at 1000 mA g^{-1}. Notably, as no foreign elements are introduced into the perovskite lattice, the A-site deficient HEPO provides a pristine platform for fundamental mechanistic studies of vacancy-driven lithium storage. This work establishes that engineering inactive A-site cation vacancies in HEPOs offers a scalable and effective paradigm for designing high-rate and durable anode materials for advanced energy storage systems.

CRediT authorship contribution statement

Aiqin Mao: Writing-original draft, Methodology, Supervision, Resources, Funding acquisition. **Feilong Yin:** Investigation, Formal analysis. **Zhengbing Wei**: Validation, Investigation, Formal analysis. Conceptualization. **MeiYi Pan and Shibiao Xu:** Supervision, Investigation. **Qianqian Hu and Zhenxing Yin:** Investigation. **Xuefeng Liu:** Writing -review & editing, Conceptualization, Supervision, Funding

Just Accepted

acquisition.

Declaration of competing interest

The authors declare that they have no known competing financial interests or personal relationships that could have appeared to influence the work reported in this paper.

Acknowledgements

This work was supported by the University Natural Science Research Project of Anhui Province in P.R. China (No 2023AH051104), the Open Project of Anhui Province Key Laboratory of Efficient Conversion and Solid-State Storage of Hydrogen & Electricity (ECSSHE2024KF05) and the Natural Science Foundation of Henan Province (262300421990).

Just Accepted

References:

[1] Lim H, Sung J, Jung J-W, et al. Design and synthesis of advanced electrode materials: from Li-ion to Na-ion batteries. *Chem Commun* 2025, **61**(83): 16150-16169.

[2] Huang L, Zhu J, Liu J-X, et al. Emerging high-entropy strategy: A booster to the development of cathode materials for power batteries. *J Adv Ceram* 2024, **13**(8): 1093-1118.

[3] Jin CQ, Tian DY, Peng ZD, et al. Interface-engineered $(CrMnTiZnCo)_3O_4$@polypyrrole nano-hybrids for superior lithium storage. *Chem Eng J* 2026, **540**: 177438.

[4] Jin CQ, Wang YL, Dong HB, et al. A Novel Spinel High-Entropy Oxide $(Cr_{0.2}Mn_{0.2}Co_{0.2}Ni_{0.2}Zn_{0.2})_3O_4$ as Anode Material for Lithium-Ion Batteries. *Inorganics* 2024, **12**(7): 198.

[5] Yao J, Wang D, Liu S, et al. High-entropy oxides anode: Exploring the high-performance application from composition design to modification strategy in lithium ion battery. *J Energy Storage* 2026, **146**: 120192.

[6] Qiu C, Li Y, Zhao X, et al. Progress on High-Entropy Oxide Anode Materials for Advanced Lithium-Ion Batteries. *ChemSusChem* 2026, **19**(4): e202502653.

[7] Ouyang B, Zeng Y. The rise of high-entropy battery materials. *Nat Commun* 2024, **15**(1): 973.

[8] Jin CQ, Wang YL, Lu P, et al. Effect of crystallite size on lithium storage performance of high entropy oxide $(Cr_{0.2}Mn_{0.2}Co_{0.2}Ni_{0.2}Zn_{0.2})_3O_4$ nanoparticles. *Electrochim Acta* 2024, **506:**.

[9] Li H, Bai Y, Feng Z, et al. Defect-engineered high-entropy spinel ferrite nanofibers via Joule

heating for superior microwave absorption. *J Adv Ceram* 2026, **15**: 9221376.
[10] Chen S, Bao M, Jia Y, et al. Lattice distortion induced rock salt high-entropy oxide for high-rate lithium-ion storage. *J Alloys Compd* 2024, **990**: 174480.
[11] Chen S, Bao M, Jia Y, et al. Boosting high-rate Li-ion storage properties by La(III) ion doping in spinel $(Co_{0.2}Cr_{0.2}Fe_{0.2}Mn_{0.2}Ni_{0.2})_3O_4$ high-entropy oxide anode. *J Adv Ceram* 2024, **13**(6): 769-779.
[12] Li C, Xiang Y, Luo B, et al. Oxygen vacancy engineering via lattice lithium pre-doping enhanced Li-ion diffusion and cycling stability in high-entropy spinel anodes. *J Energy Storage* 2026, **153**: 121132.
[13] Liu X, Ding L, Li K, et al. The role of oxygen defects in high entropy perovskite for lithium ion batteries. *Acta Materialia* 2025, **287**(287): 120812.
[14] Xu S, Wei Z, Pan M, et al. Engineering oxygen vacancies via liquid reduction for superior lithium storage in rock-salt high-entropy oxide. *J Adv Ceram* 2026, **15**(7): 9221328.
[15] Gao P, Chen Z, Gong Y, et al. The Role of Cation Vacancies in Electrode Materials for Enhanced Electrochemical Energy Storage: Synthesis, Advanced Characterization, and Fundamentals. *Adv Energy Mater* 2020, **10**(14): 1903780.
[16] Liu H, Xiao J, He H, et al. Cation-deficient perovskite $Li_{0.35}Nd_{0.55}TiO_3$ as a high-performance anode for lithium-ion batteries. *Nano Energy* 2024, **119**: 109065.
[17] Li X, Lin Z, Jin N, et al. Boosting the lithium-ion storage performance of perovskite $Sr_xVO_{3-\delta}$ via Sr cation and O anion deficient engineering. *Sci Bull (Beijing)* 2022, **67**(22): 2305-2315.
[18] Yuan D, Adekoya D, Dou Y, et al. Cation-vacancy induced Li^+ intercalation pseudocapacitance at atomically thin heterointerface for high capacity and high power lithium-ion batteries. *J Energy Chem* 2021, **62**: 281-288.
[19] Chen J, Cheng H, Li Y, et al. A-site vacancy engineering and electron density optimization in layered perovskite anodes for high-performance lithium-ion batteries. *Chem Eng J* 2025, **520**: 166231.
[20] Qing J, Mi J, Yuan J, et al. Mesoporous single-phase high-entropy oxides with abundant dual cation-anion vacancies and high surface area for enhanced CO_2 hydrogenation and CO oxidation. *Chem Eng J* 2026, **532**: 174327.
[21] Han H, Chen M, Sun C, et al. Synergy of cation/anion co-vacancy defects and cavitation for selective production and efficient utilization of H_2O_2 in water purification. *Appl Catal B Environ* 2026, **388**: 126529.
[22] Shibiao Xu , Zhengbing Wei , Mengfan Bao , et al. Cu cation vacancies enhance the lithium storage performance of perovskite-type high-entropy oxides. *CIESC Journal* 2025, **76**(12): 6718-6728.
[23] Yang L, Xiong X, Liang G, et al. Atomic Short-Range Order in a Cation-Deficient Perovskite Anode for Fast-Charging and Long-Life Lithium-Ion Batteries. *Adv Mater* 2022, **34**(17): 2200914.
[24] Wang W, Zhang Q, Jiang T, et al. Conductive $LaCeNb_6O_{18}$ with a Very Open A-Site-Cation-Deficient Perovskite Structure: A Fast- and Stable-Charging Li^+-Storage Anode Compound in a Wide Temperature Range. *Adv Energy Mater* 2022, **12**(29) : 2200656.
[25] Cao J, Wu S, He J, et al. Research progress of high-entropy perovskite oxides in energy and environmental applications: A review. *Particuology* 2024, **95**: 62-81.

Just Accepted

[26] Liu X, Ning Y, Wang M, et al. Achieving Crystal-to-Amorphous Transition without Phase Collapse in a Stable Gd-Based High-Entropy Perovskite Anode. *Nano Lett* 2026, **26**: 2184−2191.
[27] Mao A, Xiang HZ, Zhang ZG, et al. A new class of spinel high-entropy oxides with controllable magnetic properties. *J Magn Magn Mater* 2020, **497**(none): 165884.
[28] Lu Z, Ya-Ping L, Cheng L, et al. Application of $Sr_2Fe_{2-x}Mo_xO_{6-\delta}$-Based Double Perovskite Materials in Solid Oxide Cells. *Adv Ceram* 2025, **46**(06): 485-519.
[29] Yang X, Wang H, Song Y, et al. Low-Temperature Synthesis of a Porous High-Entropy Transition-Metal Oxide as an Anode for High-Performance Lithium-Ion Batteries. *ACS Appl Mater Interfaces* 2022, **14**: 26873-26881.
[30] Bao M, Chen S, Xie H, et al. Hollow/Mesoporous Spherical $La(Cr_{0.2}Fe_{0.2}Co_{0.2}Ni_{0.2}Mn_{0.2})O_3$ High-entropy Oxide Anode toward Ultrafast and Stable Lithium Storage. *J Mol Struct* 2025, **1340**: 142496.
[31] Bao M, Wei Z, Xu S, et al. Temperature-mediated crystallinity engineering in spinel high-entropy oxide anode enable high-rate pseudocapacitive lithium-ion storage. *J Power Sources* 2026, **661**: 238632.
[32] Zhang P, Gong L, Xu X, et al. Thermoelectric enhancement in A-site deficient high-entropy perovskite $(Sr_{0.25}Ca_{0.25}La_{0.25}Ba_{0.25})_{1-x}TiO_{3\pm\delta}$ ceramics by fine manipulating cation vacancies. *Chem Eng J* 2023, **472**: 144974.
[33] He J, Wang T, Bi X, et al. Subsurface A-site vacancy activates lattice oxygen in perovskite ferrites for methane anaerobic oxidation to syngas. *Nat Commun* 2024, **15**(1): 5422.
[34] Jia Y, Chen S, Shao X, et al. Synergetic effect of lattice distortion and oxygen vacancies on high-rate lithium-ion storage in high-entropy perovskite oxide. *J Adv Ceram* 2023, **12**(6): 1214-1227.
[35] Liu X, Yu Y, Li K, et al. Intergrating Hollow Multishelled Structure and High Entropy Engineering Towards Enhanced Mechano-Electrochemical Properties in Lithium Battery. *Adv Mater* 2024, **36**(19): 2312583.
[36] Li Y, Wang B, Wang Y, et al. Modulating crystal structure and lithium-ion storage performance of high-entropy oxide $(CrMnFeCoNiZn)_3O_4$ by single element extraction. *Compos Part B: Eng* 2025, **294**: 112175.
[37] Hodorová M, Csík D, Fedoročková A, et al. High-Entropy Perovskite $La(Co_{0.2}Mn_{0.2}Fe_{0.2}Ni_{0.2}Cu_{0.2})O_3$ as a Material for Lithium-Ion Batteries. *Applied Sciences* 2025, **15**(18) : 10171.
[38] Breitung B, Wang Q, Schiele A, et al. Gassing Behavior of High‐Entropy Oxide Anode and Oxyfluoride Cathode Probed Using Differential Electrochemical Mass Spectrometry. *Batteries & Supercaps* 2020, **3**(4): 361-369.
[39] Duan C, Tian K, Li X, et al. New spinel high-entropy oxides $(FeCoNiCrMnXLi)_3O_4$ (X = Cu, Mg, Zn) as the anode material for lithium-ion batteries. *Ceram Int* 2021, **47**(22): 32025-32032.
[40] Zhang N, Liu E, Chen H, et al. High-performance of $LaCoO_3/Co_3O_4$ nanocrystal as anode for lithium-ion batteries. *Colloids Surf. A: Physicochem. Eng. Asp.* 2021, **628**: 127265.
[41] Yuan L, Xu C, Zhang S, et al. Role of oxygen vacancy in spinel $(FeCoNiCrMn)_3O_4$ high entropy oxides prepared via two different methods for the selective CH bond oxidation of p-chlorotoluene. *J Colloid Interface Sci* 2023, **640**: 359-371.

Just Accepted

[42] Qin Y, Zhao H, Hua M, et al. Pseudocapacitive lithium-rich disordered rock salt vanadium oxide with 3D lithium-ion transport pathways for high-performance lithium-ion capacitor. *J. Power Sources* 2023, **588**: 233722.
[43] Sharma GP, Vikas, S. Pala RG, et al. Size induced Extrinsic Pseudocapacitance in Ultrasmall $CoMoO_4$ Nanocluster. *Energy & Fuels* 2021, **35**(23): 19765-19774.

Just Accepted